Surface diagnosis of large reflector antennas using microwave holographic metrology: An iterative approach

Y. Rahmat-Samii

Jet Propulsion Laboratory, California Institute of Technology, Pasadena

Recent investigations have shown that it is quite possible to accurately characterize the surface profile of large reflectors using microwave holographic techniques. In these techniques the complex (amplitude and phase) far-field pattern of the antenna is measured first. The surface profile is then constructed using the Fourier transform relationship which exists between the far field and a function related to the induced surface current. In this paper the concept of the Fourier transform relationship is first investigated to demonstrate that it is, in general, a summation of many Fourier transforms. However, for large reflectors with small beam widths, only the first term of the series has the major contribution. Furthermore, an iterative scheme is described to analytically/numerically continue the far-field pattern outside the measurement window. This, then, results in an improved resolution of the surface map data and, in particular, reduces the amplitude artifacts outside the boundary of the reflector. A novel and efficient simulation model has been developed to properly evaluate the accuracy of the technique in recovering the simulated surface errors. Finally, results of a recent measurement are summarized.

INTRODUCTION

Reflector surface errors can considerably affect the beam width, boresight location, gain, and side lobe structure of an antenna's radiation pattern. Today's stringent system requirements demand that the losses due to surface inaccuracies be minimized. This can be done by identifying the location and amount of distortion on the reflector surface and then by correcting them. A review of mechanical and optical surface measurement techniques for radio telescopes may be found in the works by *Findlay* [1971] and *Payne et al.* 1976]. Many of these methods can become time-consuming, especially when repeated measurements are required. Recently, considerable attention has been given to using an alternative approach based on the microwave holographic technique [*Bennett et al.,* 1976; *Scott and Ryle,* 1977; *Godwin et al.,* 1981; *Mayer et al.,* 1983] which has proven to be convenient and quick with acceptable accuracy. In this technique one measures the complex (amplitude and phase) far-field (or Fresnel zone) pattern of the antenna and then applies the Fourier transform relationship which exists between the radiation pattern and the function related to the current distribution

on the reflector surface. From the constructed phase data one can then determine the deviations of the surface from its ideal geometry. Clearly, it is desirable to limit the amount of measured data, but this can reduce resolution and can generate ambiguities in the constructed surface map. A few studies have recently been conducted to provide measurement guidelines; however, most of these studies have been based on simplified simulation models, and the possibility of using data-correcting algorithms was not fully addressed.

In this paper the concept of the Fourier transform relationship between the induced current and the far field is first investigated to demonstrate that the relationship, in general, can be interpreted as a summation of many Fourier transforms. However, for large reflectors with small beam widths, only the first term of the series has a significant contribution which allows the determination of surface errors using the Fourier transform of the far field. Furthermore, an iterative scheme similar to the one presented by *Papoulis* [1975] is used to analytically/numerically continue the far-field pattern outside the measurement window. This, then, results in an improved resolution of the surface map data and, in particular, reduces the amplitude artifacts outside the boundary of the reflector.

Simulation models have been developed to carefully study the effects of such parameters as different
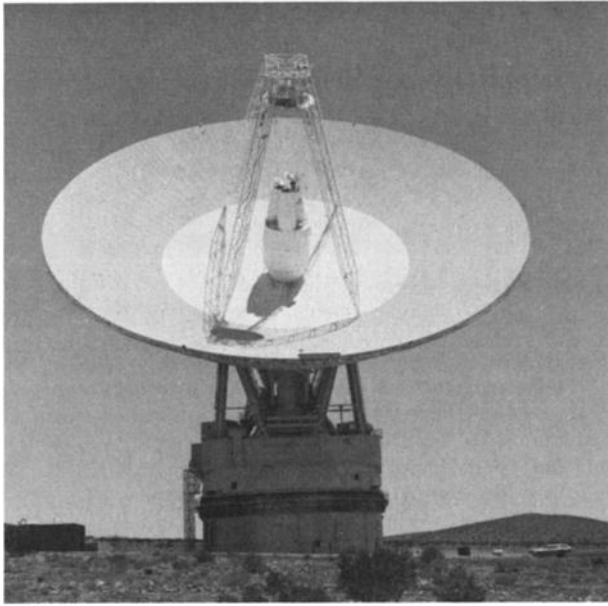
Fig. 1.   NASA/JPL 64-m deep space network reflector antenna.

surface errors (size and level), defocused feeds, pattern truncation, systematic and random errors, etc., on the accuracy of determining surface profiles. One of the models uses a tapered aperture distribution with a different circularly symmetric phase distortion. The advantage of this model is that its far field can be constructed in closed form and therefore allows a very rapid evaluation of many parameters. Other simulations use efficient numerical approaches for determining far-field patterns of curved parabolic and dual reflectors with prescribed distortions on their surfaces [*Rahmat-Samii and Galindo-Israel,* 1980, 1981; *Rahmat-Samii,* 1983a]. These approaches allow a real-life simulation for studying the effects of parameters such as feed movements, etc., on the final results. Although the methods developed in this paper are general, the numerical data are primarily presented for a reflector size corresponding to the NASA/Jet Propulsion Laboratory (JPL) 64-m deep space network (DSN) antenna. A photograph of this antenna is shown in Figure 1.

Finally, constructed surface profile maps of a recently measured DSN reflector antenna are presented [*Rahmat-Samii et al.,* 1983].

FUNDAMENTALS: SUMMATION OF FOURIER TRANSFORMS

In this section the development of the radiated pattern of a reflector based on the application of the physical optics integral is discussed. Only the final results are given, and the reader is referred to *Rahmat-Samii and Galindo-Israel* [1980] for details. The geometry of a parabolic reflector with diameter $D = 2a$ (radius a) and focal length F is shown in Figure 2. It is assumed that the reflector is illuminated by a feed located at the focal point (the off-focused feeds can be similarly discussed) and that the reflector surface may have some irregularities. Using the concept of the physical optics method, it is well known that the radiated pattern can be expressed as

$$\mathbf{E} = -jk\eta \, \frac{e^{-jkr}}{4\pi r} \, (T_\theta \hat{\theta} + T_\phi \hat{\phi}) \qquad (1)$$

where $j = (-1)^{1/2}$, $k = 2\pi/\lambda$ (λ is the wavelength), $\eta = 120\pi$ (free space impedance), and

$$\mathbf{T}(\theta, \phi) = \int_S \mathbf{J}(\mathbf{r}')e^{jkr' \cdot \hat{r}} \, dS' \qquad (2)$$

In (2), $\mathbf{J}$ is the induced surface current defined as

$$\mathbf{J} = 2\hat{n} \times \mathbf{H}^i \qquad (3)$$

where $\hat{n}$ is the surface unit normal, S is the reflector surface, and $\mathbf{H}^i$ is the incident magnetic field generated by the feed.

Integration in (2) is performed on the curved surface S with integration parameters defined on it. However, as shown by *Rahmat-Samii and Galindo-Israel* [1980], this integral can be performed in terms of the aperture coordinates (ρ', ϕ') or (x', y') by using the concept of the surface projection Jacobian. This allows one to express (2) as

$$\mathbf{T}(\theta, \phi) = \int_s \mathbf{J}(\mathbf{r}')e^{jkr' \cdot \hat{r}}J_s \, dx' \, dy' \qquad (4)$$

where the Jacobian transformation J_s is

$$J_s = \left[1 + \left(\frac{\partial f}{\partial x'}\right)^2 + \left(\frac{\partial f}{\partial y'}\right)^2\right]^{1/2} \qquad (5)$$
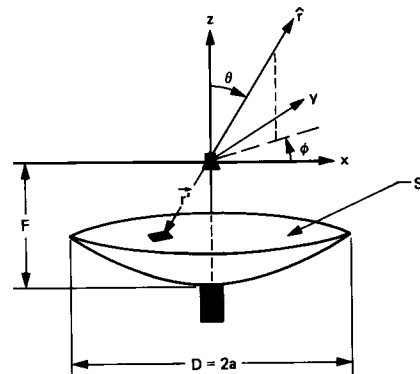

Fig. 2.   Geometry of an (equivalent) parabolic reflector.

f describes the reflector surface

$$z = f(x, y) \qquad (6)$$

and s designates the area of the projection of the reflector surface S onto the plane x-y (for symmetric reflectors this is a circular area).

Expression (4) can further be simplified by employing the following definitions and identities:

$$\mathfrak{J}(x', y') = \mathbf{J}(\mathbf{r}')J_s = 2\mathbf{N} \times \mathbf{H}^i$$

$$\mathbf{r}' \cdot \hat{r} = z' \cos \theta + ux' + vy' \qquad (7)$$

where

$$u = \sin \theta \cos \varphi \qquad v = \sin \theta \sin \varphi \qquad (8)$$

When (7) is substituted into (4), one obtains

$$\mathbf{T}(u, v) = \int_S \mathfrak{J}(x', y')[e^{jkz' \cos \theta}]e^{jk(ux' + vy')} \, dx' \, dy' \qquad (9)$$

For a flat reflector, $z' = \text{const}$, the term in the brackets will not be a function of the integration variable, and therefore $\mathbf{T}$ will be an exact Fourier transform of the induced current. However, for curved surfaces this will not, in general, be the case.

If, however, (9) is reexpressed as

$$\mathbf{T}(u, v) = \int_S \mathfrak{J}(x', y')e^{jkz'}[e^{-jkz'(1 - \cos \theta)}]e^{jk(ux' + vy')} \, dx' \, dy' \qquad (10)$$

(10) can then be expanded in terms of the Taylor series for small values of θ, namely,

$$\mathbf{T}(u, v) = \sum_{p=0}^{P \to \infty} \frac{1}{p!} [-jk(1 - \cos \theta)]^p \mathbf{T}_p \qquad (11)$$

where

$$\mathbf{T}_p = \int_S z'^p \mathfrak{J}(x', y')e^{jkz'}e^{jk(ux' + vy')} \, dx' \, dy' \qquad (12)$$

Notice that (11) is now a summation of Fourier transforms with its dominant term expressed as

$$\mathbf{T}(u, v) = \int_S \mathfrak{J}(x', y')e^{jkz'}e^{jk(ux' + vy')} \, dx' \, dy' \qquad (13)$$

The contribution of higher-order terms in the series expansion of (11) becomes significant for wide-angle observations (large θ) and laterally displaced feeds. In the work by Rahmat-Samii and Galindo-Israel, [1980], many examples are demonstrated which show the importance of the higher-order terms in predicting the reflector patterns. However, as far as the scope of this paper is concerned, the only important term is $\mathbf{T}_0$ (renamed $\mathbf{T}$ in (13) for simplicity).

Once $\mathbf{T}$ is determined, the far-field pattern can then be obtained from (1). In many cases, $\mathbf{T}$ may be determined by its Cartesian components T_x, T_y, and T_z, which can be transformed to the spherical components by

$$\begin{Bmatrix} T_\theta \\ T_\phi \end{Bmatrix} = \begin{pmatrix} \cos \theta \cos \phi & \cos \theta \sin \phi & -\sin \theta \\ -\sin \phi & \cos \phi & 0 \end{pmatrix} \begin{Bmatrix} T_x \\ T_y \\ T_z \end{Bmatrix} \qquad (14)$$

Furthermore, application of Ludwig's third definition [*Ludwig*, 1973] allows the definition of the copolar and cross-polar components of the far-field pattern as

$$\begin{Bmatrix} T_{\text{copol}} \\ T_{\text{cross-pol}} \end{Bmatrix} = \begin{pmatrix} \sin \phi & \cos \phi \\ \cos \phi & -\sin \phi \end{pmatrix} \begin{Bmatrix} T_\theta \\ T_\phi \end{Bmatrix} \qquad (15)$$

In (15) it is assumed that the radiated field is predominantly y-polarized. For the x-polarized field case, the rows of the square matrix in (15) must be interchanged. From (14) and (15) it can be shown that for the cases where θ is small, the following holds:

$$\begin{Bmatrix} T_{\text{copol}} \\ T_{\text{cross-pol}} \end{Bmatrix} \cong \begin{Bmatrix} T_y \\ T_x \end{Bmatrix} \qquad \text{small } \theta \qquad (16)$$

The application of the reciprocity theorem implies that the transmitting and receiving patterns are identical. Therefore if the reflector antenna of Figure 2 is impinged by a plane wave, the output at the feed port will be proportional to the antenna receiving pattern for a given direction of incidence and plane wave polarization. For the sake of simplicity, it is assumed that the dominant polarization is in the y direction, and therefore, by using (16) and (13), the following expression for the pattern is obtained:

$$T = \int_S \mathfrak{J}(x', y')e^{jkz'}e^{jk(ux' + vy')} \, dx' \, dy' \qquad (17)$$

Notice that the vector notations are removed in (17), in order to emphasize that only one polarization is considered.

CONSTRUCTION OF SURFACE PROFILE

Expression (17) relates the Fourier transform of a function, which is related to the induced current, to the far-field pattern. Obviously, the domain of integration in (17) only extends to the region where current exists, namely, the reflector surface. Note that although (17) resembles the aperture integration formulation, it is very different, in that the induced current is still on the reflector surface, not on the projected aperture. In order to demonstrate that the sur-
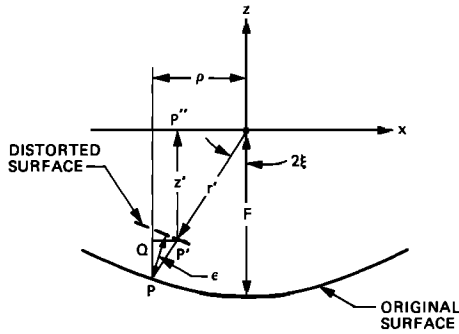
Fig. 3. Enlargement of surface distortion.

face profile information can be extracted from (17), let it first be assumed that the phase center of the feed is located at the focal point and that the surface irregularities are described by function $\varepsilon(x, y)$ in the normal direction, namely,

$\varepsilon(x, y)$ = surface irregularity in the normal direction

An enlarged view of an irregularity is depicted in Figure 3. It is observed in this figure that for small surface distortions the following holds:

$$P'P + PQ = \frac{\varepsilon}{\cos \xi} + \frac{\varepsilon}{\cos \xi} \cos 2\xi = 2\varepsilon \cos \xi \qquad (18)$$

where for a parabolic reflector,

$$\cos \xi = \left(1 + \frac{\rho^2}{4F^2}\right)^{-1/2} = \left(1 + \frac{x^2 + y^2}{4F^2}\right)^{-1/2} \qquad (19)$$

The term inside (17) may now be expressed as

$$\tilde{J}(x', y')e^{jkz'} = |\tilde{J}(x', y')| e^{-jkr'}e^{jkz'} \qquad (20)$$

Note that the phase term exp $(-jkr')$ is obtained from (3) because the phase center of the feed is located at the focal point. The exponents in (20) can now be expressed as

$$-r' + z' = -r' - P'P''$$

$$= -r' - P'P'' - P'P - PQ + P'P + PQ \qquad (21)$$

For a parabolic reflector,

$$-r' - P'P'' - P'P - PQ = -2F \qquad (22)$$

which finally results in

$$-r' + z' = -2F + 2\varepsilon \cos \xi \qquad (23)$$

If the total distortion phase error is defined as

$$\delta = 4\pi(\varepsilon/\lambda) \cos \xi \qquad (24)$$

(17) can then be expressed as

$$T(u, v) = e^{-j2kF} \int_S |\tilde{J}(x', y')| e^{j\delta}e^{jk(ux' + vy')} \, dx' \, dy' \qquad (25)$$

The constant phase term exp $(-j2kF)$ in (25) is the result of erecting the center of the coordinate system at the focal point. Different phase constants can result if the center of the coordinate system is displaced from this focal point. It should also be noticed that both copolar and cross-polar patterns can be used to determine δ from (25).

If both the amplitude and the phase of the reflector pattern T are measured (or simulated), the surface distortion can be determined from (25) via an inverse Fourier transform, namely,

$$|J(x, y)| e^{j\delta} = e^{j2kF} \mathscr{F}^{-1}[T(u, v)] \qquad (26)$$

where $\mathscr{F}$ designates the Fourier transform.

By using (26), (24), and (19), the surface distortion $\varepsilon(x, y)$ in terms of the wavelength is finally obtained as

$$\frac{\varepsilon(x, y)}{\lambda} = \frac{1}{4\pi} \left(1 + \frac{x^2 + y^2}{4F^2}\right)^{1/2} \text{phase } \{e^{j2kF} \mathscr{F}^{-1}[T(u, v)]\} \qquad (27)$$

In constructing $\varepsilon(x, y)$ from (27), the constant and linearly dependent phase terms in the braces must first be extracted. These phase terms account for the ambiguity in defining the phase reference and the beam displacement due to lateral feed displacement. It is also possible to identify the best fit quadratic dependence which could be used to remove the feed axial defocusing by readjusting the feed position. Similar expressions can also be constructed for Cassegrainian reflectors using the concept of equivalent paraboloid. For these reflectors, the effects of the blockage may be interpreted in terms of shadowing in the induced current. Additional work may be needed to properly account for the effects of the blockage diffraction.

SAMPLING THEOREM

Since the integrand of (17) has a finite support (reflector surface), its Fourier transform T is an analytic function which extends to infinity. Conversely, since the transform of T is a function with a finite support, the sampling theorem can be invoked to express $T(u, v)$ by only its values at the sampling points. For a reflector with diameter D, the sampling

interval is

$$\text{largest sampling interval} = \frac{1}{D/\lambda} \qquad (28)$$

which is closely related to the reflector beam width (uniform illumination case). However, since the fast Fourier transform (FFT) algorithm is used to evaluate (26), intervals smaller than the largest sampling interval must be used to overcome the aliasing problem. For this reason the parameter κ is introduced which typically is in the range of $0.5 < \kappa < 1$. The sampling interval is then given by

$$\Delta u = \Delta v = \frac{\kappa}{D/\lambda} \qquad (29)$$

The value $\varepsilon(x, y)/\lambda$ from (27) can be determined almost exactly, provided the pattern $T(u, v)$ is known in its entirety (infinitely extended) and with an acceptable level of snr (signal-to-noise ratio). In practice, this is not the case, and $T(u, v)$ is measured or simulated only in a finite range. If the total number of measured (simulated) data in each of the u and v directions is designated by N_{MSR}, then the total number of measured data is

$$N_{\text{MSR}} N_{\text{MSR}} = (2N + 1)(2N + 1) \qquad (30)$$

The variable N is introduced in (30) to denote the number of measured data to one side of the boresight (see Figure 4). Similarly, the total number of points used to perform FFT can be defined as

$$\text{total number of points for FFT} = N_F N_F \qquad (31)$$

For the cases when $N_F > N_{\text{MSR}}$, however, the domain of the measured pattern must be extended, as discussed in the next section.

Since (27) is evaluated using FFT, the values of $\varepsilon(x, y)$ are determined at the intervals to be

$$\Delta x = \frac{D}{\kappa(N_F - 1)} \qquad \Delta y = \frac{D}{\kappa(N_F - 1)} \qquad (32)$$

However, as far as the actual surface resolutions for identifying the surface errors are concerned, the parameter N_{MSR} is a more dominant factor than N_F.

It is worthwhile to mention that in many measurement configurations it may not be possible to measure $T(u, v)$ at rectangular grid points in (u, v) space, but rather in other convenient coordinates. For these configurations, FFT cannot be directly used until the data are rearranged with an interpolation algorithm. An alternative would be to evaluate the double summation resulting from the discrete Fourier representation of (17) in a numerical manner, which would take, however, longer computation time than the FFT evaluation.
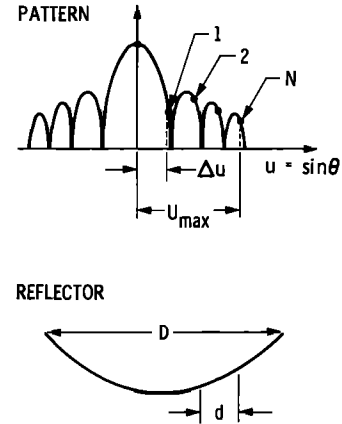

Fig. 4. Sampling points of the reflector antenna far-field pattern. Surface resolution is $d \approx D/(2N\kappa)$, and error in determining the surface distortion ε is $\Delta\varepsilon \approx 2N\lambda/(4\pi\text{snr})$ where snr is the signal-to-noise ratio at the boresight.

ITERATIVE SCHEME

In many cases, it may be necessary to extend the domain of the measured (simulated) data $T(u, v)$ in order to possibly improve the achievable resolution. There are many different algorithms available which use a variety of concepts to extend the measured (simulated) pattern beyond the measurement range. One of these methods, which appears to be very promising, uses an iterative approach similar to the one discussed by Papoulis [1975]. The steps of this iterative procedure as applied to microwave holography are presented here.

First, (17) is reexpressed as

$$T(u, v) = \mathscr{F}[Q] = \int_s Q(x', y')e^{jk(ux' + xy')} \, dx' \, dy' \qquad (33)$$

Since Q is zero outside the reflector boundary (assuming neither a ground reflection nor any outside obstacles), the domain of integration in (33) can be extended to infinity, and hence the Fourier transform relationship holds. The function Q is constructed from T using the relation

$$Q(x, y) = \mathscr{F}^{-1}[T] \qquad (34)$$

Since T is only given in the measurement domain, the iterative procedure is used to extend this domain, with the steps depicted in Figure 5. The procedure starts by filling in zeros in the desired extended
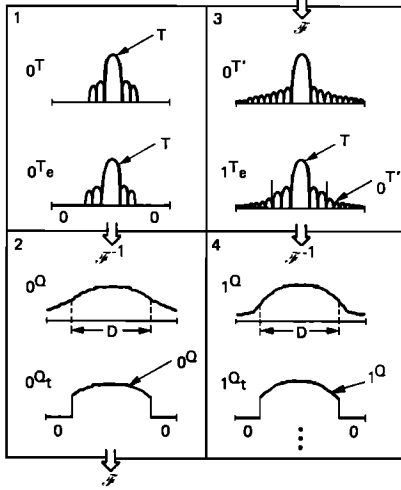
Fig. 5. Steps of the iterative scheme. T is the measured or simulated far-field pattern, and $_0Q$ is the amplitude profile.

domain to give the zeroth iterated extended pattern $_0T_e$ such that it takes the same value as T inside the original domain and zero value outside, namely,

$$_0T_e = T \quad \text{in the original domain}$$
$$_0T_e = 0 \quad \text{in the extension} \tag{35}$$

Next, the inverse Fourier transform (using FFT) is used to find $_0Q(x, y)$, the zeroth iteration of $Q(x, y)$. Obviously, since $_0T_e$ is a truncated function, its transform will extend to infinity. However, it is known from the physics of the problem that $_0Q(x, y)$ should only be extended within the region where the antenna surface exists. This information is next used to truncate $_0Q(x, y)$ to the domain of the antenna (radius $D/2$). Once the truncated version of $_0Q$, namely $_0Q_t$, is constructed, then a forward transform is taken to obtain $_0T'$. From T and $_0T'$ the first iterated form of T, namely $_1T_e$, is constructed such that

$$_1T_e = T \quad \text{in the original domain}$$
$$_1T_e = _0T' \quad \text{in the extension} \tag{36}$$

It is clear that $_1T_e$ is an improvement over $_0T_e$, since its extended domain is filled with a nonzero function. The inverse Fourier transform of $_1T_e$ is denoted by $_1Q$, and this process is followed for higher orders of iterations. Parseval's theorem can be used to show that the tail end of function $Q(x, y)$ gradually diminishes outside the physical domain of the antenna, which is a manifestation of the convergence of the procedure. Once the nth iterative value of Q is deter-

mined, $Q(x, y)$ can then be determined from (27). In the next section the use of this iterative procedure will be demonstrated in several numerical examples.

APERTURE SIMULATION MODEL

The purpose of this model is to simulate an aperture distribution with a prescribed amplitude taper and phase irregularities, in accordance with the reflector illumination and surface irregularities. The model assumes that both the amplitude and the phase are circularly symmetric. This assumption allows one to construct the far-field pattern in a closed form which can then be sampled at designated intervals. The application of FFT to these sampled data finally results in the recovery of the simulated surface distortion. A comparison of the recovered and simulated surface distortion is the basis for judging the effects of parameters such as sampling intervals, number of samples, etc., on the accuracy of the technique. A block diagram of the steps used in this section is shown in Figure 6, which also indicates the possibility of using a more sophisticated curved reflector diffraction model and adding systematic and random noises from an error simulator.

Formulation

The geometry of a circular aperture with different annular regions is shown in Figure 7, where the radii of these regions are designated by $a_0, a_1, a_2, \cdots$, $a_N = a$ (a_0, in this figure, is used to designate the
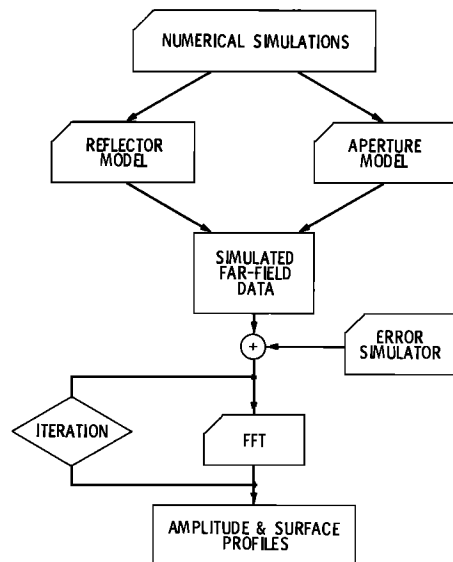

Fig. 6. Schematic of the numerical simulation. Broken-corner rectangles represent the developed computer programs.

central blockage region). Let us assume that the amplitude and phase distributions across the aperture are given by Q and δ, respectively, and that these functions are circularly symmetric. The far-field pattern of this aperture distribution is constructed using the Fourier transform in polar coordinates to obtain

$$T = \int_{a_0}^{a} \int_{0}^{2\pi} Q(\rho')e^{j\delta(\rho')}$$

$$\cdot \{\exp\left[jk\rho' \sin\theta \cos(\phi - \phi')\right]\}\rho' \, d\rho' \, d\phi' \quad (37)$$

with the inner region having radius a_0 considered as the blockage region ($a_0 = 0$, no blockage).

It is further assumed that $\delta(\rho')$ takes the constant value δ_n in the nth annular region, which can be interpreted as the phase irregularity (surface irregularity) in the nth annular region. With this assumption, (37) may be expressed as

$$T = \sum_{n=1}^{N} T_{n,n-1} e^{j\delta_n} \quad (38)$$

with

$$T_{n,n-1} = T_n - T_{n-1} \quad (39)$$

$$T_n = 2\pi \int_{0}^{a_n} Q(\rho')J_0(k\rho' \sin\theta)\rho' \, d\rho' \quad (40)$$

with J_0 being the zero-order Bessel function.

The aperture amplitude distribution is defined as

$$Q(\rho) = B + C\left[1 - \left(\frac{\rho}{a}\right)^2\right]^P \quad B + C = 1 \quad (41)$$

where parameter B is used to control the edge taper, namely,

$$\text{edge taper} = 20 \log B \quad (42)$$

It has been found that for values of $1 \le P \le 2$, (41) is an adequate representation of the aperture amplitude distribution for many typical reflectors. In this study, the values of $P = 1$ and 2 are used, as (40) can be integrated in a closed form [Rahmat-Samii, 1983b]. To arrive at this, the following identity is used:

$$I_p(\alpha) = 2 \int_{0}^{1} x^{2p+1}J_0(\alpha x) \, dx$$

$$= \frac{2}{\alpha} J_1(\alpha) - p\left(\frac{2}{\alpha}\right)^2 J_2(\alpha) + p(p-1)\left(\frac{2}{\alpha}\right)^3 J_3(\alpha) - \cdots \quad (43a)$$

$$I_p(0) = \frac{1}{p+1} \quad (43b)$$

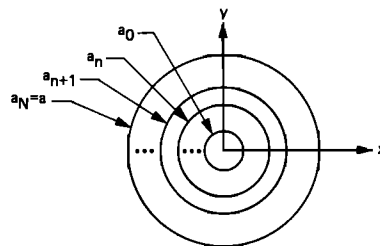Substituting (41) into (40), using (43) and introduc-

Fig. 7. Circular aperture with annular phase distortions.

ing the notation

$$u_n = ka_n \sin\theta \quad (44)$$

one finally arrives at

$$P = 1: T_n = \pi a_n^2 \left\{ B \frac{2}{u_n} J_1(u_n) + C\left[\frac{2}{u_n} J_1(u_n)\right.\right.$$

$$\left.\left. - \frac{a_n^2}{a^2}\left(\frac{2}{u_n} J_1(u_n) - \left(\frac{2}{u_n}\right)^2 J_2(u_n)\right)\right]\right\} \quad (45a)$$

$$P = 1: T_n(0°) = \pi a_n^2 \left[B + C\left(1 - \frac{a_n^2}{2a^2}\right)\right] \quad (45b)$$

$$P = 2: T_n = \pi a_n^2 \left\{ B \frac{2}{u_n} J_1(u_n) + C\left[\frac{2}{u_n} J_1(u_n) - \frac{2a_n^2}{a^2}\right.\right.$$

$$\cdot \left(\frac{2}{u_n} J_1(u_n) - \frac{4}{u_n^2} J_2(u_n)\right) + \frac{a_n^4}{a^4}\left[\frac{2}{u_n} J_1(u_n)\right.$$

$$\left.\left.\left. - 2\left(\frac{2}{u_n}\right)^2 J_2(u_n) + 2\left(\frac{2}{u_n}\right)^3 J_3(u_n)\right]\right]\right\} \quad (46a)$$

$$P = 2: T_n(0°) = \pi a_n^2 \left[B + C\left(1 - \frac{a_n^2}{a^2} + \frac{a_n^4}{3a^4}\right)\right] \quad (46b)$$

Expressions (45) and (46) can be used to construct the far field from (38). In order to further relate the aperture phase error to the reflector surface distortion, the following value for δ_n is used:

$$\delta_n = 4\pi \frac{\varepsilon_n}{\lambda}\left(1 + \frac{\tilde{a}_n^2}{4F^2}\right)^{-1/2} \quad (47)$$

where ε_n and $\tilde{a}_n$ are the surface error in the normal direction and the average radius of the nth zone, respectively, namely,

$$\tilde{a}_n = \frac{a_n + a_{n-1}}{2} \quad (48)$$

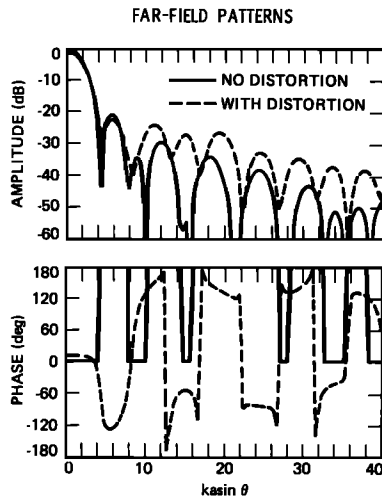and F is the focal length of the parabola as shown in Figure 3.

FAR-FIELD PATTERNS

Fig. 8. Far-field patterns of the nondistorted (solid curves) and distorted (dashed curves) reflector with parameters given in (50).

Numerical results and discussion

Many numerical results have been constructed on the basis of the simulated model of this section. However, for the sake of brevity, only a few representative results are discussed, which demonstrate the usefulness of the aperture model and the utility of (27) in recovering the surface profile. Although all the formulations are very general, the numerical results are tailored to the reflector geometrical configuration, which closely resembles the equivalent parabola related to the DSN 64-m antenna of Figure 1. The operation frequency is chosen at S band, namely,

$$f = 2.281 \text{ GHz} \qquad \lambda = 13.15 \quad \text{cm} \qquad (49)$$

At this frequency the reflector parameters are

a/λ radius, equal to 243.3;
F/λ equivalent focal length, equal to 1030.56;
a_0/λ blockage radius, equal to 25.5;
 ET   edge taper, equal to -10 dB;
 $P = 1$ (equation (41)).

A computer program has been generated on the basis of the mathematical developments of the previous sections. In one case, far-field patterns are constructed for the reflector with no surface profile errors and, in another case, with surface profile errors as follows:

$$
\begin{array}{ll}
\varepsilon_1/\lambda = 0 & 25.5 < \rho/\lambda < 80 \\
\varepsilon_2/\lambda = 0.02 & 80 < \rho/\lambda < 100 \\
\varepsilon_3/\lambda = 0 & 100 < \rho/\lambda < 150 \qquad (50) \\
\varepsilon_4/\lambda = 0.10 & 150 < \rho/\lambda < 180 \\
\varepsilon_5/\lambda = 0 & 180 < \rho/\lambda < 243.3
\end{array}
$$

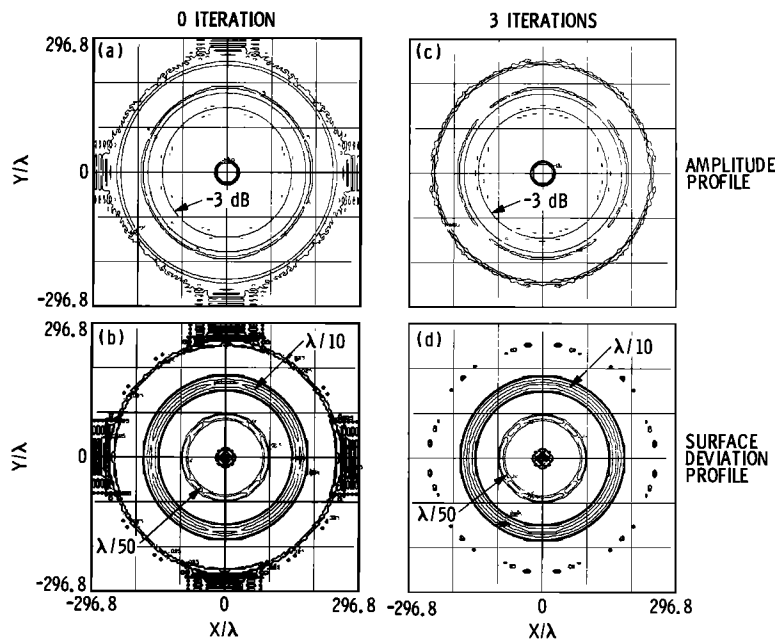Note that the above surface profile designates two

Fig. 9. Constructed amplitude and surface distortion profiles for the simulated distortion: (a–b) results of zero iteration, (c–d) results after three iterations.
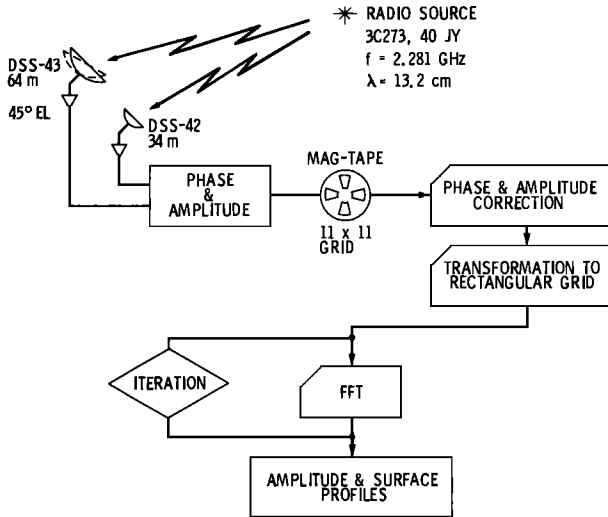
Fig. 10.   Schematic of the measurement and surface profile construction steps.

annular rings of width 20λ and 30λ with surface errors of $\lambda/50$ and $\lambda/10$, respectively. The amplitude and phase patterns are shown in Figure 8. These results demonstrate the effects of the simulated surface profile distortions on the patterns.

On the basis of these simulated patterns, one can then evaluate the accuracy of the holographic technique by trying to recover the simulated surface profile for different parameters, such as the sampling in-

terval, number of sampled points, etc. The results of one such simulation are shown as aperture amplitude and surface profile contour maps in Figures 9a–9d. For this case, the sampling interval is

$$\Delta u = \kappa \frac{\lambda}{2a} = 0.81 \times 0.00206 \qquad (51)$$

Results clearly indicate that for the employed number of sampling and FFT points (i.e., $N_{MSR} = 63$, $N_F = 128$ in this case), the simulated surface profile has been recovered very well. Furthermore, application of the iteration scheme has reduced the amplitude artifacts outside the reflector boundary considerably (Figures 9c–9d). However, if a grid of 11×11 sampling points had been used, the annular ring of 20λ and the subreflector could not have been recovered. Many simulations have been performed by systematically and randomly contaminating the far-field values at the sampling points to determine what these effects are on the reconstructed surface profile.

It is worthwhile to mention that for a prescribed surface distortion the constructed far-field patterns are exact as far as the aperture model is concerned and, furthermore, are obtained without using FFT. This is an improvement over previously reported simulation techniques where FFT was used to construct the far-field pattern. The FFT is used here only
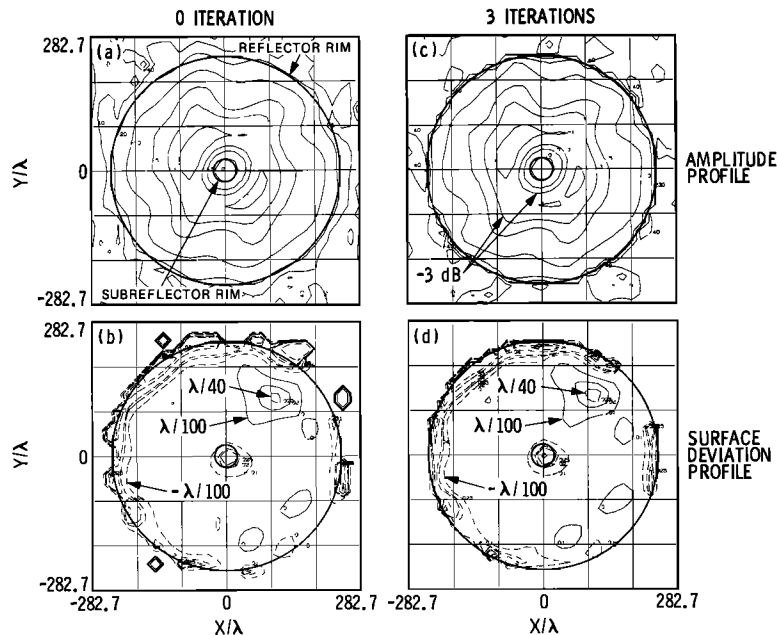

Fig. 11.   Constructed amplitude and surface distortion profiles from the measured data taken from the 64-m DSN antenna at 2.28 GHz: (a–b) results of zero iteration, (c–d) results after three iterations.

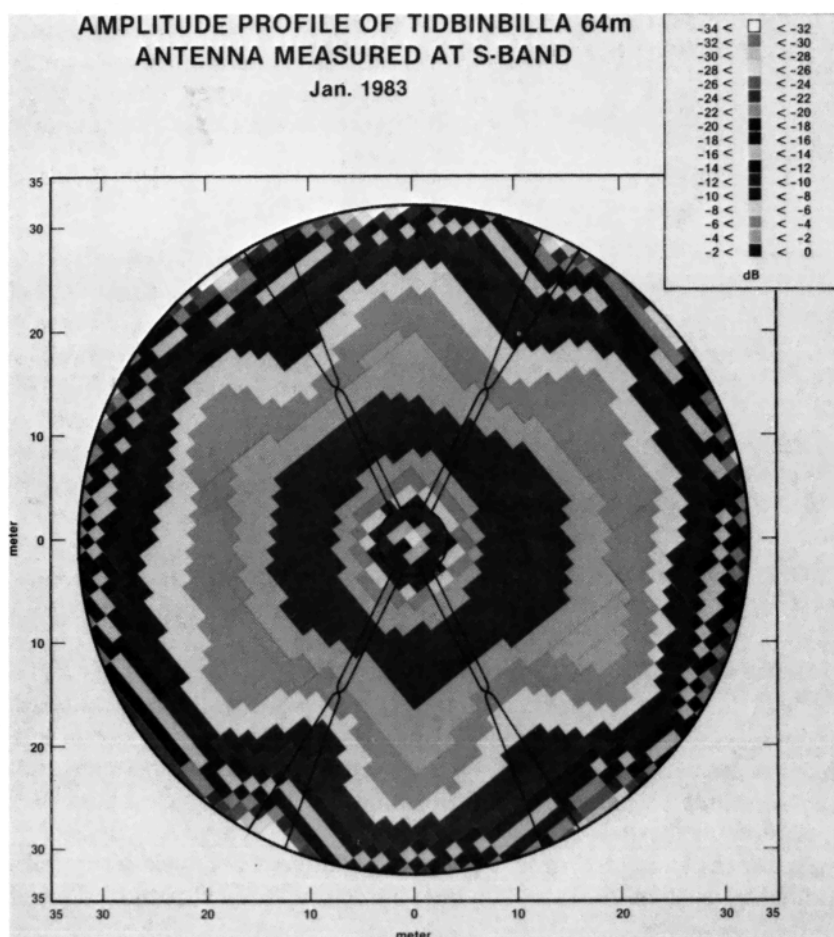## AMPLITUDE PROFILE OF TIDBINBILLA 64m ANTENNA MEASURED AT S-BAND
Jan. 1983

Fig. 12a.   False color representation of the constructed aperture amplitude profile from the measured data.

to recover the surface profile from the closed-form constructed far-field pattern.

RESULTS OF A MEASUREMENT

In this section a summary of the recent holography measurement of one of the NASA/JPL DSN antennas is presented [Rahmat-Samii et al., 1983]. Only some preliminary results are shown here, and more details will be presented in future papers. To perform a holography measurement, in practice, a second antenna is needed to provide a phase reference. This can often be a small and low-cost design antenna. In the case of many radio astronomy installations, the reference antenna may already exist if the antenna to be measured belongs to an array. The test and reference antennas are typically illuminated at a single frequency using a terrestrial, satellite-borne, or celestial radiation source of small angular diameter. This technique has been used by various researchers to

measure a number of antennas, using frequencies over the range 5 to 86 GHz. The accuracy attainable depends on a number of factors, including the signal-to-noise ratio, tropospheric phase fluctuations, pointing stability, instrumental effects, etc.

A measurement was performed at 2.28 GHz (13.15 cm) on the DSN 64-m antenna stationed in Tidbinbilla, Australia (called DSS-43), using the 34-m antenna (called DSS-42), as the reference antenna. Data were acquired while offsetting the 64-m antenna in a rectangular grid path, centered at the position of the compact radio source 3C273, which has a flux density of about 40 Jy (40×10^{-26} W m^{-2} Hz^{-1}), and tracked in an elevation angle range of about 40° to 55° for various sets of measurements. The beam of the 34-m antenna was kept centered on the radio source. The measured data, which were obtained using the connected-element interferometer procedure, consisted of 11×11 sampling grid points at
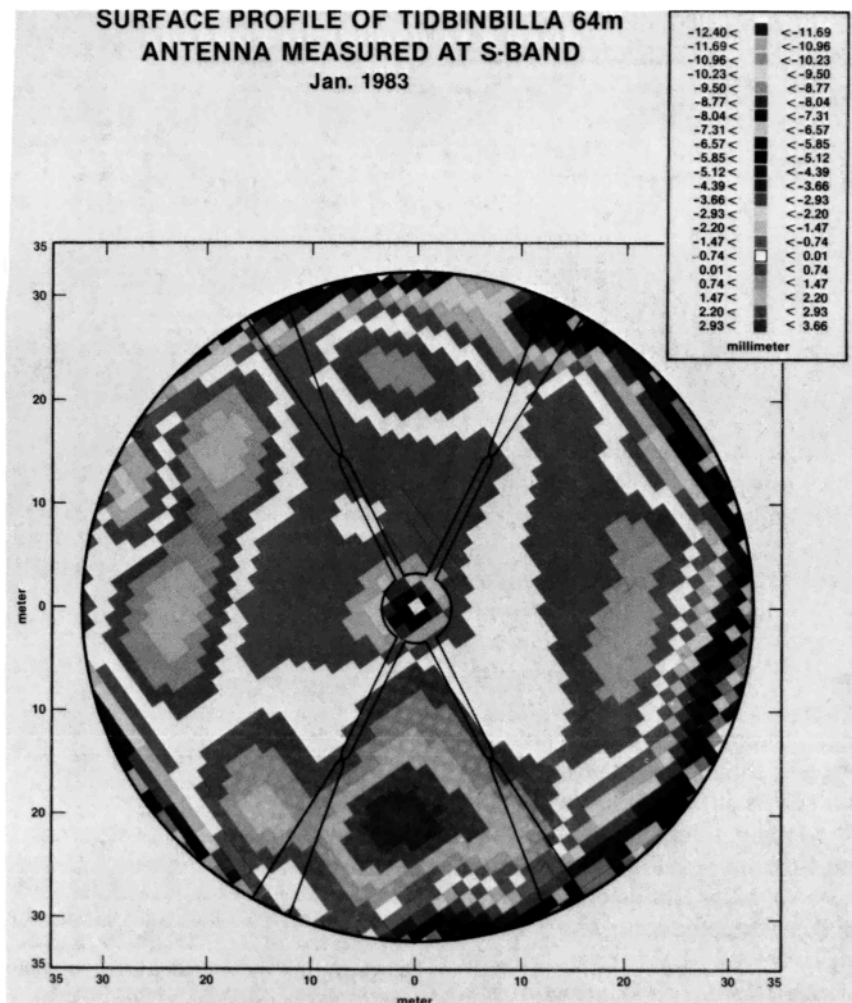
Fig. 12b. False color representation of the constructed surface distortion profile from the measured data.

5.7 arc min spacings with dwell times of 10 s at each point. In addition, the 64-m antenna was periodically returned to the central grid position, to ensure a continuous calibration of the instrumental gain and phase. The entire grid was measured in 70 min. The schematic of the measurement setup and the data processing algorithm are shown in Figure 10.

After removing a slow phase drift and amplitude fluctuation using calibration points, the processed data yielded phase and amplitudes accurate to approximately 2° and 2%, respectively. These data were then used as input to the computer program to finally result in the reflector surface profile. Results are shown in Figures 11a–d for amplitude and surface profile contours for both zero and three iteration steps. The iterated scheme clearly defines the boundary of the reflector and reduces the amplitude arti-

facts outside the reflector boundary. False color maps were also constructed of the reflector's amplitude and surface profiles as shown in black and white pictures in Figures 12a and 12b. The coordinates of these maps were rotated with respect to the contour maps of Figures 11a–11d in order to present a better match between them and the structural orientation of the antenna. Although the resolution of this initial experiment is fairly coarse (i.e., an 11 × 11 matrix), several features emerge from these maps. First, the constructed amplitude profiles show a signature of the subreflector and quadripod legs with a certain degree of clarity. Furthermore, the surface profile maps suggest that there may be a general surface distortion of about 3 mm near two feet of the quadripod legs. Additional surface distortions are observed in a region near the edge of the reflector. Over most
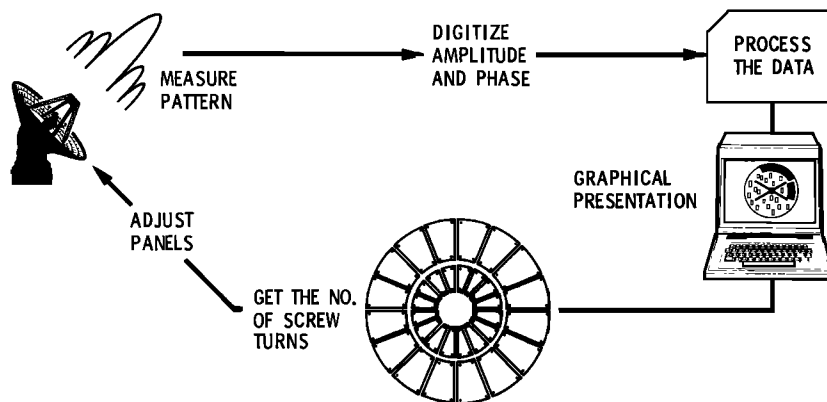
Fig. 13.   Block diagram of the microwave holographic surface adjustment procedure.

of the reflector surface the distortion is below a level of about 1 mm and is noticeably less over the central region of the reflector. The unweighted rms surface deviation from this measurement is about 1.8 mm, and when weighted by the radial amplitude taper, it is about 1.1 mm, which agrees well with a previously estimated value based on the reflector efficiency.

In a time difference of approximately 1.5 hours, a second connected-element measurement was conducted in the exact manner as in the first experiment. The results obtained compared very well with results of the first experiment in both amplitude and surface profile maps. The only major difference between maps was an axial rotation of about 17.5°, which resulted from the change in the source location during the time period between the two experiments. The results of the second experiment and their comparisons with the first have been reported by this author in two JPL internal documents.

It must be emphasized that the results from both of these measurements are preliminary and further investigation will be conducted to refine them by perhaps using stronger sources such as satellites with the objective of achieving a spatial resolution of 0.4 m and an rms surface precision of 0.5 mm using 201 × 201 measured points with an snr (signal-to-noise ratio) of 63 dB (at 7.7 GHz) or 74 dB (at 2.2 GHz). Finally, it is hoped that the holographic procedure will be used routinely at different DSN sites in order to check the surface condition of the reflectors and adjust the displaced panels in accordance with the block diagram of Figure 13.

REFERENCES

Bennett, J. C., A. P. Anderson, P. A. McInnes, and A. J. T. Whitaker, Microwave holographic metrology of large reflector antennas, *IEEE Trans. Antennas Propag.*, AP-24, 295–303, 1976.

Findlay, J. W., Filled-aperture antennas for radio astronomy, *Annu. Rev. Astron. Astrophys.*, 9, 271–292, 1971.

Godwin, M. P., A. J. T. Whitaker, J. C. Bennett, and A. P. Anderson, Microwave diagnostics of the Chilbolton 25 m antenna using the OTS satellite, paper presented at International Conference, Inst. of Electr. Eng., York, England, 1981.

Ludwig, A. C., The definition of cross polarization, *IEEE Trans. Antennas Propag.*, AP-21, 116–119, 1973.

Mayer, C. E., J. H. Davis, W. L. Peters, and W. J. Vogel, A holographic surface measurement of the Texas 4.9-meter antenna at 86 GHz, *IEEE Trans. Instrum. Meas.*, IM-32, 102–109, 1983.

Papoulis, A., A new algorithm in spectral analysis and band-limited extrapolation, *IEEE Trans. Circuits Syst.*, 22, 735–742, 1975.

Payne, J. M., J. M. Hollis, and J. W. Findlay, New method of measuring the shape of precise antenna reflectors, *Rev. Sci. Instrum.*, 47, 50–55, 1976.

Rahmat-Samii, Y., Effects of deterministic surface distortions on reflector antenna performance, paper presented at Symposium on Electromagnetic Theory, URSI, Santiago de Compostela, Spain, 1983a.

Rahmat-Samii, Y., An efficient computational method for characterizing the effects of random surface errors on the average power pattern of reflectors, *IEEE Trans. Antennas Propag.*, AP-31, 92–98, 1983b.

Rahmat-Samii, Y., and V. Galindo-Israel, Shaped reflector antenna analysis using the Jacobi-Bessel series, *IEEE Trans. Antennas Propag.*, AP-28, 425–435, 1980.

Rahmat-Samii, Y., and V. Galindo-Israel, Scan performance of

dual offset reflector antennas for satellite communications, *Radio Sci., 16,* 1093–1099, 1981.

Rahmat-Samii, Y., S. Gulkis, S. G. Levy, B. L. Seidel, L. E. Young, M. J. Batty, and D. L. Jauncey, Microwave holographic surface measurement of the Tidbinbilla 64 meter antenna, paper presented at Meeting of Astronomical Society of Australia, Sydney, 1983.

Scott, P. F., and M. Ryle, a rapid method for measuring the figure of a radio telescope reflector, *Mon. Not. R. Astron. Soc., 178,* 539–545, 1977.

Y. Rahmat-Samii, Jet Propulsion Laboratory, California Institute of Technology, Pasadena, CA 91109.